Received: 13 August 2024 | Revised: 19 November 2024 | Accepted: 18 December 2024

DOI: 10.1002/jex2.70031

TECHNICAL REPORT

Quantitative fluorescent nanoparticle tracking analysis and nano-flow cytometry enable advanced characterization of single extracellular vesicles

Danilo Mladenović[1,2] | **Joseph Brealey**[3] | **Ben Peacock**[3] | **Kairi Koort**[2] | **Nataša Zarovni**[4]

[1]HansaBioMed Life Sciences OÜ, Tallinn, Estonia

[2]School of Natural Sciences and Health, Tallinn University, Tallinn, Estonia

[3]NanoFCM Co., Ltd., Nottingham, UK

[4]RoseBio, Milano, Italy

Correspondence
Danilo Mladenović, HansaBioMed Life Sciences OÜ, Tallinn, Estonia. Email: danilo@hansabiomed.eu

Funding information
Tallinn University Research Fund, Grant/Award Number: TF7320; Ettevõtluse Arendamise Sihtasutus, Grant/Award Number: 2014-2020.4.02.21-0398 (EVREM); Eesti Teadusagentuur, Grant/Award Number: TT11 (ELIXIR)

Abstract

Current state-of-the-art tools for analysing extracellular vesicles (EVs) offer either highly sensitive but unidimensional bulk measurements of EV components, or high-resolution multiparametric single-particle analyses which lack standardization and appropriate reference materials. This limits the accuracy of the assessment of marker abundance and overall marker distribution amongst individual EVs, and finally, the understanding of true EV heterogeneity. In this study, we aimed to define the standardized operating procedures and reference material for fluorescent characterization of EVs with two commonly used EV analytical platforms—nanoparticle tracking analysis (NTA) and nano-flow cytometry (nFCM). We achieved quantitative fluorescence analyses on ZetaView NTA and NanoAnalyzer nFCM instruments, by utilizing yellow-green FluoSpheres (FS) with assigned ERF (equivalent reference fluorophore) values. This standardization technique allowed for fluorescent EV signal to be expressed in ERF units (indicative of bound fluorescent antibodies per EV), thus enabling measurement of target protein marker abundance on individual EVs, and in the whole EV population. The NTA's and nFCM's limits of detection (LoD) were evaluated at 21 and 9 Alexa Fluor 488 (AF488) molecules, respectively. To complement the limited quantification of markers expressed in a few copies per single EV, in-line bulk fluorescence measurements with a plate reader were performed. This provided absolute marker quantification and more insightful analyses of EV heterogeneity and marker stoichiometry. The standardization method outlined in this work unlocks the full analytical potential of NTA and nFCM, enabling cross-platform data comparison. At the same time, it highlights some of the technical challenges and considerations and thus contributes to the ongoing efforts towards the development of EV analytical tools.

KEYWORDS

characterization, extracellular vesicles, fluorescent labelling, FluoSpheres, nano-flow cytometry, nanoparticle tracking analysis, standardization

1 | INTRODUCTION

Over the past decade, we have witnessed a rise, and a great expansion of advanced platforms and tools for analyses of EVs (Hendrix et al., 2023). From bulk assays, which usually provide high sensitivity but unidimensional measurements, the analyses have reached down to a single particle level, opening the possibility for multiparametric assessment of individual EVs, and a deeper understanding of their heterogeneity and complexity (Bagci et al., 2022; Hilton & White, 2021; Kwon & Park, 2022; Zhu et al., 2023). These systems allow simultaneous biophysical and biochemical evaluation of EVs by measuring their size, concentration, charge, morphology, refractive index, and/or composition. The latter is often achieved via fluorescent reagents that target different components (lipids, proteins, nucleic acids, metabolites, etc.), present either on the membrane or within the lumen of EVs (Bao et al., 2023; Fortunato et al., 2021). A common strategy, offering great flexibility and value for EV characterization, utilizes antibodies labelled with various fluorochromes, to detect a rich display of proteins on the EV surface. This enables phenotyping of different EV subpopulations, to determine their putative cellular or subcellular origin, and also offers the potential for biomarker discovery, making possible EV-based diagnostics (Bobrie et al., 2012; van Niel et al., 2018).

Even though state-of-the-art instruments for single particle analyses offer higher resolution compared to the bulk assays, their true potential for EV phenotyping is often downplayed by the lack of standardized protocols and reference materials. Popular methods, such as nanoparticle tracking analysis (NTA), nano-flow cytometry (nFCM), or even super-resolution microscopy and on-chip fluorescence imaging capable of single-molecule sensitivity, are currently achieving qualitative or semi-quantitative analyses, at best (Breitwieser et al., 2022; Choi et al., 2019; Fortunato et al., 2021; Lee et al., 2018; McNamara et al., 2022). Quantitative single molecule localization microscopy (qSMLM) possesses unparalleled analytical power for quantification of marker abundance per individual EVs (Lennon et al., 2019; Saftics et al., 2023). However, fluorescent NTA (FNTA) and nFCM offer greater flexibility and high throughput multiparametric analyses, making them preferred tools for day-to-day use in EV research. Even if more conventional, FNTA and nFCM are still not standardized, or at least not yet widely adopted for fluorescent quantification of EV content, although, efforts in this direction were made in the past (Chen et al., 2015; Gao et al., 2021). Choice of calibrators, which would unlock their full quantitative potential, is reduced to the well-established MESF (molecules of equivalent soluble fluorophore) beads, used in the traditional flow cytometry (Welsh et al., 2023; Welsh et al., 2020). However, the fluorescence they emit is orders-of-magnitude brighter than the fluorescent signal we might expect from any labeled EV. In turn, this requires data extrapolation outside of the calibrated quantification range, producing estimates which have much higher uncertainty (Lozano-Andrés et al., 2024; Welsh et al., 2023). Smaller and dimmer hard-dyed beads assigned with ERF values may provide a suitable alternative for fluorescence calibration. However, they usually have spectrally mismatched multi-peak emission, with respect to the fluorochromes used in EV labelling, which limits their application (Hoffman et al., 2012).

In this work, we defined the analytical protocols and evaluated the performance of two commonly used instruments for single EV analyses—Particle Metrix ZetaView and NanoFCM NanoAnalyzer. We employed yellow-green FluoSpheres (FS) hard-dyed beads, with single-peak AF488-like emission spectra, for standardizing fluorescence readout in ERF units and estimating the instruments' sensitivity levels. To demonstrate the method's utility, EVs purified from simple (cell-conditioned media) and complex (blood plasma) biofluids were used for analysing multiple markers and their abundance per single EV and in the whole EV population, via AF488-labeled antibodies. Finally, we complemented the single-particle analyses of FNTA and nFCM with high-sensitivity bulk fluorescence measurements performed using a plate reader, to overcome the individual limitations of each platform and obtain more comprehensive results.

2 | MATERIALS AND METHODS

2.1 | Extracellular vesicles (EVs) derived from COLO cell line

Colorectal cancer COLO205 cell culture media was processed by differential centrifugation (300 × *g* for 10 min and 1600 × *g* for 15 min, at 4°C) and tangential flow filtration (TFF-MVs with a pore size of ~150–200 nm; HansaBioMed Life Sciences, Estonia, product code HBM-TFF-MV). The TFF-MVs retentate containing medium-sized EVs larger than ~150-200 nm was referred to as COLO mEVs (Lyophilized Microvesicles from COLO1 cell line; HansaBioMed Life Sciences, product code HBM-mvCOLO-50). The TFF-MVs permeate containing particles smaller than ~150–200 nm was further purified with size exclusion chromatography (SEC) column (maxiPURE-EVs; HansaBioMed Life Sciences, product code HBM-mxPEV-3) to obtain small EVs, referred to as COLO sEVs (Lyophilized Exosomes from COLO1 cell line; HansaBioMed Life Sciences, product code HBM-COLO-100/2). The EV quality was assessed by NTA, BCA, and sandwich ELISA EV marker analyses (the certificates of analyses are provided in the Supplementary Material). Subsequently, both sEVs and mEVs were used for staining with fluorescent antibodies, as described below.

2.2 | Blood plasma processing and EV purification

A healthy donor blood plasma pool (50 donors), containing EDTA as an anticoagulant, was purchased from BioIVT (Human Plasma K2EDTA; BioIVT, United Kingdom, product code HUMANPLK2PNN). The plasma was obtained from the whole blood within 15 min after the collection by centrifugation at 2800 × *g* for 20 min in a refrigerated centrifuge (5°C) to remove platelets. The platelet-depleted plasma was then frozen and shipped with appropriate cold chain handling. Before the experiments, the plasma was thawed and immediately centrifuged for 15 min at 2500 × *g*, at 4°C, in 50 mL Falcon tubes (Corning, United States of America, product code 352070), followed by filtration through a 0.45 μm PES syringe filter (Minisart; Sartorius, Germany, product code 16537). Such precleared plasma was then used for EV purification.

PURE-EVs SEC column (HansaBioMed Life Sciences, product code HBM-PEV-5) was equilibrated with particle-free PBS without calcium and magnesium (Corning, product code 21-031-CV). For EV purification, 2 mL of precleared plasma was loaded on top of the column, and fractions of 0.5 mL were collected in 1.5 mL microtubes (Eppendorf, Germany, product code EP0030108116). The elution profile of plasma EVs was previously determined by NTA, BCA, and ELISA EV marker analyses (Mladenović et al., 2023). Thus, the fractions 6–11 (3 mL) containing EVs were pooled in a 15 mL Falcon tube (Corning, product code 352096) and used for staining with fluorescent antibodies.

2.3 | EGFP fluorescent EVs

Commercially available EVs derived from transfected HEK293 cell line overexpressing EGFP (enhanced green fluorescent protein)-conjugated CD63 (FLuoEVs; HansaBioMed Life Sciences, product code HBM-HEK-EGFP63) were purified from the cell culture media by differential centrifugation (300 × *g* for 10 min, 1600 × *g* for 15 min, and 10,000 × *g* for 30 min, all at 4°C) and maxiPURE-EVs SEC column. Thus obtained FLuoEVs were used for direct analyses on FNTA to define the traces-to-particles (T:P) ratio criteria. Furthermore, FLuoEVs were used to assess the effect of different FNTA threshold levels (minimum brightness) on event detectability and overall analysis outcome.

2.4 | Silica and polystyrene beads

Monodisperse 105.1 nm (Corpuscular, Canada, product code 147020-10) or polydisperse 68, 91, 113, and 155 nm size standard silica beads in 1:1:1:1 particle ratio (NanoFCM Silica Nanospheres Cocktail #1; NanoFCM Inc., China, product code S16M-Exo) were used for comparison of particle concentration and size measurements in scatter mode of NTA and nFCM.

Yellow-green FS carboxylate-modified microspheres of 100, 40, and 20 nm (Thermo Fisher Scientific, United States of America, product codes F8803, F8795, and F8787) were used for assigning the number of antibody equivalents. Subsequently, they were used as reference material for fluorescence analyses on FNTA, nFCM, and plate readers. A detailed description of the methodology is provided in separate sections.

2.5 | Staining EVs with fluorescent antibodies

EVs were stained using the antibodies described in Table 1. Staining reactions for fluorescence analyses were prepared in PBS, according to Table 2. Incubation was carried out at 37°C (for COLO EVs) or at room temperature (for plasma EVs), in 0.5 mL microtubes (Eppendorf, product code 0030124537), covered from light, under continuous low-speed shaking for 1.5 h. Afterwards, the unbound antibodies were removed as previously described (Fortunato et al., 2021). Briefly, samples were washed with 450 μL PBS using Nanosep centrifugal devices with Omega membrane 300K (Cytiva, United States of America, product code OD300C34) and centrifugation at 3000–5000 × *g*, until most of the liquid had passed in the permeate. After 6 washing cycles, the retentate was recovered in ~100–110 μL of PBS and analyzed on NTA, nFCM, and plate reader. PBS only, dye only, and EVs only (unstained) were used as process controls and for background subtraction, as recommended by MISEV and MIFlowCyt-EV guidelines (Welsh et al., 2024; Welsh et al., 2020).

2.6 | Assignment of antibody/AF488/EGFP equivalents to FS beads

The fluorescence of yellow-green FS beads and AF488-labeled antibodies was measured with a plate reader in order to convert the arbitrary units of fluorescence intensity of FS beads into the number of antibody equivalents. First, FS beads and antibodies were serially diluted in PBS and loaded in a black polystyrene 96-well plate with no binding capacity (Biomat, Italy, product code

TABLE 1 Antibodies used for EV staining.

Sample	Antibody description	Provider
COLO sEVs and COLO mEVs	Human CD9 Alexa Fluor 488-conjugated antibody, IgG2B (product code FAB1880G)	Bio-Techne R&D Systems (United States of America)
	Human CD63 Alexa Fluor 488-conjugated antibody, IgG1 (product code IC5048G-100UG)	
Plasma EVs	Human CD9 Alexa Fluor 488-conjugated antibody, IgG1 (product code A4-208-T100)	Exbio (Czech Republic)
	Human CD63 Alexa Fluor 488-conjugated antibody, IgG1 (product code A4-343-T100)	
	Human Integrin alpha 2b/CD41 Alexa Fluor 488-conjugated antibody, IgG1 (product code FAB7616G-100UG)	Bio-Techne R&D Systems
	Human Glycophorin A Alexa Fluor 488-conjugated antibody, IgG1 (product code FAB1228G-100UG)	

Abbreviation: EV, extracellular vesicles.

TABLE 2 EV staining reactions.

Staining reaction	Volume [µL]	Number of particles	Antibody [µg]
COLO sEVs	40	5×10^9	0.8
COLO mEVs	40	2.5×10^9	0.8
Plasma EVs	100	5×10^9	0.25

Abbreviation: EV, extracellular vesicles.

MGB03F2-NB). The measurements were performed on a GENios Pro microplate reader (Tecan Group Ltd., Switzerland) with a 485 nm excitation wavelength, and emission was detected through a 535/25 nm bandpass filter. The number of FS beads per well was calculated based on the bead concentration provided by the manufacturer. The number of antibodies per well was calculated based on the antibody concentration provided by the manufacturer (µg/mL), molecular weight (IgG ~150 kDa = 150,000 g/mol), and Avogadro's constant (6.022×10^{23} molecules/mol). For example, 10 ng of antibody translates to ~4×10^{10} IgG molecules. After subtracting the blank (PBS), the plate reader data (fluorescence intensity), the number of beads per well, and the number of antibodies per well were log-transformed, and linear regression was plotted using antibodies as a reference. From the obtained equation, the fluorescence intensity of the FS beads was converted to the number of equivalent fluorescent antibodies. This was done for each individual antibody type and lot, due to the differences in antibody production and subsequent fluorophore-to-protein (F:P) ratios. All of the serial dilutions and measurements were performed in at least three independent experiments, to obtain the average number of antibody molecules per bead (Supplementary Material 1). The standard deviation was on average 9% (2%–15% range). Following the principles previously reported (Buranda et al., 2011; Cook et al., 2023; Görgens et al., 2019), additional correction factors were applied to these calculations to compensate for the differences in optical configurations between the instruments (plate reader, FNTA, and nFCM), and slight spectral mismatching of AF488 and FS beads. Equations and detailed information are provided in the Supplementary Material 2 and Figure S1. The excitation/emission spectra of fluorophores, and excitation and collection efficiencies of different optical configurations, were obtained from https://www.fpbase.org/spectra/ (Lambert, 2019; Lambert, 2023). For FNTA, a correction factor of ×1.17 was applied to the number of antibodies assigned per each FS bead using a plate reader, while for nFCM, the correction factor was ×1.04.

Using the known F:P ratio for multiple different antibodies (provided by the antibody manufacturers, Supplementary Material 1), the assigned antibody equivalents per each FS bead were converted to AF488 equivalents.

To further convert the signal to EGFP equivalents per FS bead, the intensity and spectral differences between AF488 and EGFP were taken into account, and the correction factor of ×1.66 was calculated for FNTA optical configuration (Supplementary Materials 1 and 2).

2.7 | Nanoparticle tracking analyses

Particle Metrix Zeta View PMX-120 NTA instrument with 488 nm laser (Particle Metrix, Germany) was used for single-particle analyses in scatter and fluorescence mode. Instrument setup was done according to the manufacturer's guidelines (cell check and auto-alignment with 100 nm polystyrene beads standards upon each start-up). For analyses in scatter mode, camera sensitivity

was set at 85, shutter speed at 100, with high video quality at 30 frames/s, minimal area 10, maximal area 10,000, minimum brightness 20, and minimum trace length 15. Fluorescence measurements of FS beads and fluorescent EVs were carried out using a 500 nm long-pass filter, with the camera sensitivity set at 95, shutter speed at 100, low video quality at 30 frames/s, minimal area 10, maximal area 1000, minimum brightness varying between 20, 25, 30, and 35 (depending on the background level, and desired T:P ratio), minimum trace length set at 5, and with 'Low Bleach' technology enabled. PBS was used as a diluent for every NTA analysis.

FS beads were measured in each experiment using the same protocol as for stained EVs (described above), and FCS files were exported. In case of multiple measurements of a single sample, FCS files were merged using an online tool floreada.io/fcsmerge, to obtain a unified file for all the traces acquired per sample. The FCS files were then opened using floreada.io/analysis, and a custom parameter for fluorescence intensity 'FI[log10]' was created using the formula *log10({Mean Intensity}*{Area})*. The gating was performed for each bead population. This was particularly necessary for FS100 since their fluorescence intensity was too high, causing the beads that were out of focus to still 'peek' into the focal plane, appearing as dimmer events (Figure S2). The median fluorescence intensity (MFI) was calculated for each gated population and statistics were exported (function 'Save CSV statistics file'). MFI was then used together with the assigned antibody, AF488, or EGFP values corrected for the FNTA (see Assignment of antibody/AF488/EGFP equivalents to FS beads), and linear regression was plotted. The equation thus obtained was then used to estimate the number of bound antibodies (type and lot specific), AF488, or EGFP molecules, respectively, per each traced fluorescent event. An example of Excel formulae used for analyses of FCS files of stained EV samples is provided in Supplementary Material 3.

When analyzing stained EV samples in fluorescence mode, minimal criteria were established—to acquire at least 300 total traces per analyzed sample, and the T:P ratio had to be ≥35% (i.e., 300 traces per ~850 analyzed particles), comparable to the one obtained in scatter mode. The former was achieved by running multiple acquisitions and injecting more concentrated samples into the FNTA cell (if the fluorescent events were scarce, like in plasma EV samples). The desired T:P ratio was obtained by reanalyzing the video file of the same sample with a minimum brightness set at 20, 25, 30, or 35. Finally, the traces collected in FCS files were used for further analyses.

For the results summary of scatter measurements, particle concentration (subtracted by blank) was obtained from the 11-position table, while median and average particle size were calculated from the FCS files. For fluorescence measurements, particle concentration was subtracted by blank and additionally unstained samples, if there were any detectable autofluorescent particles. The median and average particle size and the number of antibodies per particle were computed from the FCS files using the Excel formulae in Supplementary Material 3.

2.8 | nFCM

A NanoAnalyzer U30 instrument (NanoFCM Inc.) equipped with dual 488/640 nm lasers was used for the simultaneous detection of side scatter (SSC) and fluorescence of individual particles. Single-photon counting avalanche photodiode detectors (SPCM APDs) with bandpass filters allowed for collection of light in specific channels (SSC–488/10 nm; FL1–525/40 nm; FL2–670/30 nm). The sampling pressure by air pump module was 1 kPa, the sheath fluid was gravity-fed HPLC-grade water, and measurements were taken over 60 s. Values for peak height (mean + 3 standard deviations of the background) and peak width (0.3 ms) were used as thresholds for peak identification.

For each particle, peak area was recorded in all three detection channels simultaneously, for use in constructing dot plots and histograms. Samples were diluted to attain a particle count within the optimal range of 1500–12,000/min. Blank measurements of TE buffer (10 mM Tris, 1 mM EDTA) were recorded, containing 200–400 particles/min, these particles were subtracted from the sample measurement for concentration calculation. In the fluorescence measurements, additional subtractions were performed using the unstained control samples, if there were any detectable autofluorescent events.

Particle concentrations were determined by comparison to a standard containing 250 nm silica nanoparticles of known concentration. Particles were sized according to standard operating procedures using a proprietary 4-modal NanoFCM Silica Nanospheres Cocktail #1. Using the NanoFCM software (NanoFCM NF Profession V2.0), a standard curve was generated based on the intensity of side scattered light of the four different silica particle populations of 68, 91, 113, and 155 nm in diameter. The laser was set to 15 mW and 10% SSC decay.

FS beads were measured in each experiment using the same protocol as for the stained EVs. MFI of each bead population was used in combination with the assigned antibody values corrected for the nFCM (correction factor ×1.04, see Assignment of antibody/AF488/EGFP equivalents to FS beads), and linear regression was plotted. The equation thus obtained was used to estimate the number of bound antibodies (type and lot specific) per each detected fluorescent event.

Data processing was handled within the NanoFCM NF Profession V2.0 software, with dot plots, histograms, and statistical data provided in a single PDF. Gating within the software allows for proportional analysis of subpopulations separated by fluorescent intensities.

2.9 | Microplate reader

The bulk fluorescence measurements were performed using a GENios Pro microplate reader with a detection limit of 0.4 femtomoles of fluorescein per well. The excitation wavelength was 485 nm, and the emission was detected through a 535/25 nm bandpass filter. Stained and washed EVs (5×10^8–8×10^9 particles/well, depending on the sample) were loaded in a black polystyrene 96-well plate with no binding capacity and diluted with PBS up to 100 µL. The same number of unstained EVs or the same volume of blank controls were loaded in the plate and used to subtract the background. All controls produced a negligible amount of background noise, that is, comparable to PBS. As a reference, serially diluted FS beads were loaded and measured in parallel to produce a standard curve (with the log-transformed data) based on the previous antibody assignments. The equation of this linear regression was then used to calculate the number of antibodies in our samples (expressed as antibodies/µL of the sample). For comparison, antibody concentration in a sample was also estimated from FNTA and nFCM measurements by multiplying the average number of antibodies/particle (average epitope abundance) with the fluorescent particle concentration.

2.10 | BCA protein assay

The protein concentration was determined using Pierce BCA Protein Assay Kit (Thermo Fisher Scientific, product code 23227), by following the manufacturer's instructions. Briefly, 10–25 µL of samples or BSA standards were loaded into the Nunc 96-well polystyrene round bottom plate (Thermo Fisher Scientific, product code 268152). Reagent A and reagent B from the assay kit were mixed to prepare a BCA working reagent (50 parts of reagent A with 1 part of reagent B), and 200 µL of the working reagent were added to each well-containing sample or BSA standard. After thorough mixing, the plate was covered and incubated at 37°C for 30 min. The absorbance was measured at 560 nm on a GENios Pro microplate reader. The raw data of the BSA standards were used to plot the linear regression and calculate the protein concentration in the EV samples.

2.11 | ELISA

Sandwich ELISA and ELISA in a high-binding plate were used for the analyses of purified EVs. COLO sEVs (20 µL) were diluted in PBS up to 100 µL and loaded in the 96-well plate coated with anti-CD63 antibody (ExoTEST; HansaBioMed Life Sciences, product code HBM-RTK-CMK) for the analysis of CD9, CD63, and CD81 marker expression. COLO mEVs (10 µL) were diluted in PBS up to 100 µL and loaded in the 96-well plate with high-binding capacity (Biomat, product code MG01F-HB8) for the analysis of CD9 and CD63 marker expression. Plasma EVs (25, 12.5, and 6.25 µL) were diluted in PBS up to 100 µL and loaded in the 96-well plate with high-binding capacity for the analysis of GYPA and CD41 marker expression. Anti-human CD9, CD63, and CD81 biotin-conjugated mouse monoclonal antibodies (included in the ExoTEST kit) were diluted 1:500 in the sample buffer (SB; included in the ExoTEST kit), while anti-human GYPA and CD41 (Bio-Techne R&D Systems, product codes FAB1228G-100UG and FAB7616G-100UG) were diluted 1:100. HRP-conjugated streptavidin (included in the ExoTEST kit) diluted 1:5000 in SB, and HRP-conjugated rabbit-anti-mouse secondary antibody (included in the ExoTEST kit) diluted 1:2000 in SB were used accordingly. Sample and antibody incubation, washing steps, incubation with ELISA substrate, and signal detection were carried out following the ExoTEST protocol. Absorbance was measured at 450 nm with GENios Pro microplate reader.

2.12 | Data analyses

FCS files from FNTA were analyzed using the Floreada.io online tool and Excel formulae in Supplementary Material 3. NFA files from nFCM were analyzed using the NanoFCM NF Profession V2.0 software. All the results are shown as the mean ± SD, $n \geq 3$. The data were analyzed and the figures were plotted using GraphPad Prism 10.4.0.

3 | RESULTS

3.1 | Comparative detection of synthetic nanoparticles across EV analysis platforms

To first compare the performance of NTA in scatter mode (SNTA), and nFCM in particle sizing and quantification, monodisperse (105.1 nm) and polydisperse (68, 91, 113, and 155 nm in a 1:1:1:1 ratio) size standard silica beads were analyzed. For this purpose, the same settings were used for the analysis of EVs in scatter mode. Both instruments produced similar measurements of concentration and size for monodisperse beads, although the latter was significantly lower compared to the beads rated value (Figure 1a).

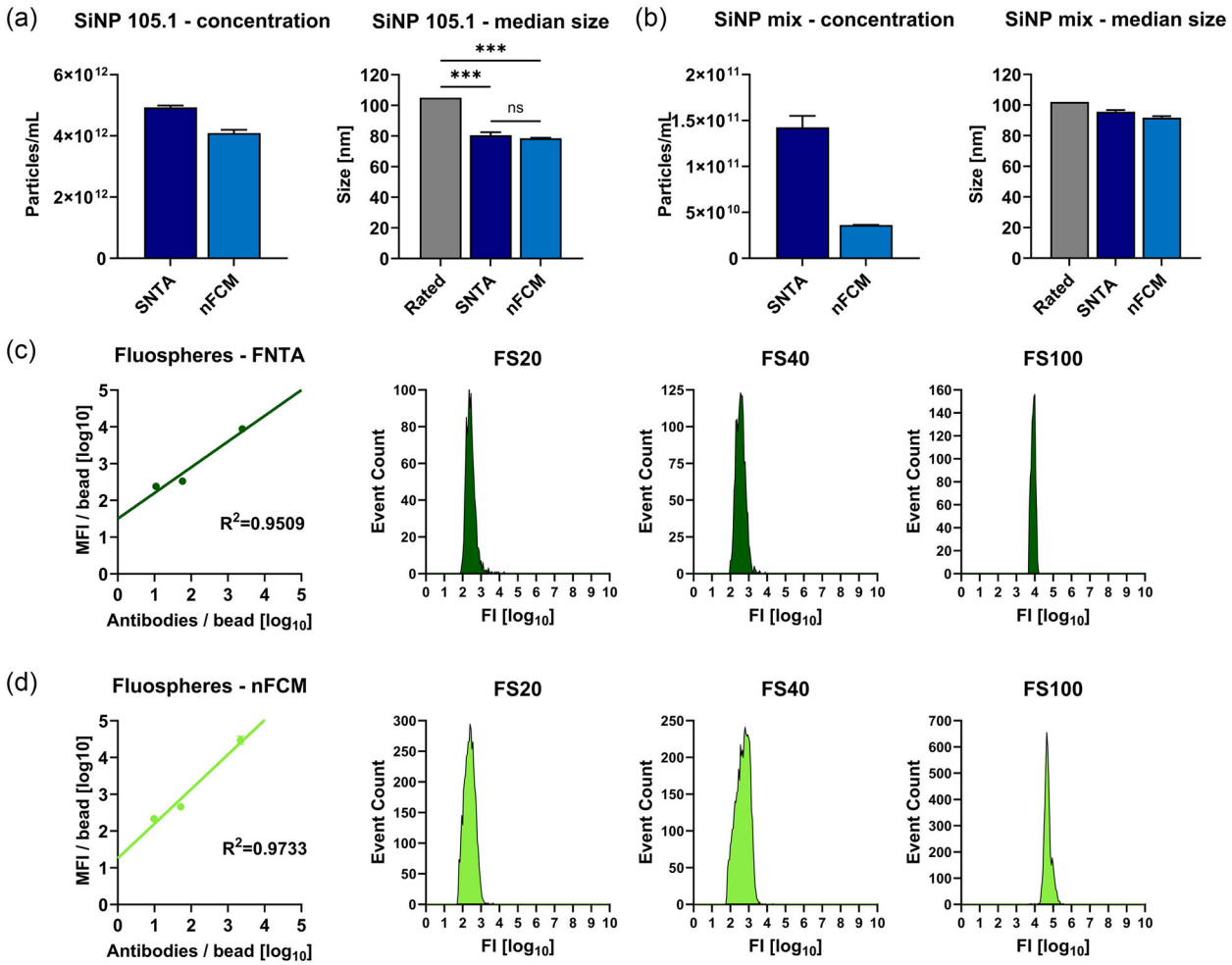

FIGURE 1 Silica and FS beads. Silica bead size standards in (a) monodisperse (105.1 nm) and (b) polydisperse suspensions (68, 91, 113, and 155 nm in a 1:1:1:1 particle ratio) were measured on SNTA and nFCM. Additional PSD histograms are shown in the Figure S3. FS of different sizes (20, 40, and 100 nm) and fluorescence intensities were analyzed on (c) FNTA and (d) nFCM, and used to plot a linear regression with MFI on Y-axis and number of AF488-labeled antibodies on X-axis in $\log_{10}$ scale (provided example is for anti-CD9-AF488 antibody used in COLO sEV experiments). The MFI was calculated from separate measurements of each type of FS beads, as shown in the representative histograms. Number of antibody equivalents per bead was assigned separately with a plate reader by measuring serially diluted FS beads against each antibody used in this study, and by applying the correction factors according to the optical configuration of each instrument (Supplementary Materials 1 and 2). Data are shown as the mean ± SD of at least three independent experiments. Statistical significance was analyzed using ordinary one-way ANOVA with Tukey's test for multiple comparisons (alpha = 0.05, $p = 0.1234$ [ns], 0.0332 [∗], 0.0021 [∗∗], 0.0002 [∗∗∗], < 0.0001 [∗∗∗∗]). FNTA, fluorescent NTA; FS, FluoSpheres; SNTA, NTA in scatter mode; MFI, median fluorescence intensity; nFCM, nano-flow cytometry; NTA in scatter mode; PSD, particle size distribution.

This discrepancy can be explained by the fact that the bead's rated size comes from a DLS measurement, which is a method known to provide a bias towards larger particles (Filipe et al., 2010). With polydisperse silica beads, the concentration appeared approximately 4-fold higher on SNTA (Figure 1b). This observation is in line with prior reported overestimation in SNTA concentration measurements of polydisperse samples (Vogel et al., 2021). Nevertheless, the estimated median size remained similar between SNTA and nFCM, and concordant with the rated value, in spite of SNTA's inability to discern individual subpopulations of different sizes (Figure S3).

For comparison of instruments' performances in fluorescence mode, fluorescent polystyrene FS beads of three different sizes (~100, 40, and 20 nm) and brightness levels were used. First, the beads were assigned the ERF value, by measuring them with the microplate reader against the serial dilutions of AF488-labeled antibodies used in the subsequent experiments. Thus, the FS fluorescence intensity was expressed as the number of equivalent antibody molecules per bead (Supplementary Material 1). Due to the differences in F:P ratios (i.e., different amounts of conjugated AF488 molecules per antibody), the assignment had to be done separately for each antibody type and production lot used in this study. Correction factors were devised to compensate for slight differences in the excitation and collection efficiencies of optics in microplate reader, FNTA, and nFCM, as described in the Materials and Methods (subchapter Assignment of antibody/AF488/EGFP equivalents to FS beads) and Supplementary Material 2. Marginal mismatching in excitation/emission spectra of the FS and AF488 was also taken into consideration. Thus,

after the ERF assignment was done by a microplate reader, a correction factor of ×1.17 was applied to the number of assigned antibodies for FNTA, and ×1.04 for nFCM (Figure S1, Supplementary Materials 1 and 2).

The MFI of the beads measured on either FNTA or nFCM was converted to $\log_{10}$ scale and linear regression was plotted against the assigned ERF values, expressed in $\log_{10}$ as well (Figure 1c, d). Since the fluorescence intensity is not a native parameter of FNTA, it was calculated by multiplying the *Area* and *Mean Intensity* of each detected event in the FCS file, followed by calculating the MFI of the whole population (Supplementary Material 3). As shown in the representative linear regression plotted for anti-CD9 antibody (Figure 1c, d), nFCM displayed higher linearity between the data points, and better resolution, evidenced by a steeper slope. Since antibody assignment had to be done for each antibody type and production lot, individual linear regressions and equations were plotted and used for ERF conversions in the subsequent experiments.

3.2 | Optimizing NTA settings to define analytical acceptance criteria

When specific post-acquisition parameters (e.g., minimum and maximum particle area and brightness) are used in NTA measurements (either in scatter or fluorescence mode), the particles fitting the given criteria are detected and reported in the total particle concentration (particles/mL). However, only a fraction of these particles are successfully traced to acquire additional information, such as particle size and brightness (scattered light or fluorescence), which is then extrapolated to represent the total particle population. If the acquired T:P ratio is low, due to the low particles' brightness (Figure 2a), or if the T:P is inconsistent between the measurements, this can introduce bias in the analyses. The shift in the T:P ratio can be especially noticeable with fluorescent particles which are dimmer and more difficult to detect (and trace) than scattering events.

Thus, to define the T:P acceptance criteria and maintain reliability between our acquisitions and downstream result interpretation, we analyzed commercially available FLuoEVs (fluorescent EVs with CD63-EGFP) in both scatter and fluorescence mode, using variable Minimum Brightness thresholds while keeping all other parameters unchanged. The amount of EGFP molecules per single EV was determined as described in Materials and Methods. As shown in Figure 2b, the number of particles and traces detected in the scatter mode scaled proportionally with the increase of the brightness threshold level, which allowed the T:P ratio to be maintained at ∼35% at all times. The traces that were lost in the higher threshold levels were, as expected, the smaller EVs, evidenced by the increased median particle size.

When FLuoEVs were analyzed in the fluorescence mode (FNTA, Figure 2c) with different Minimum Brightness thresholds, the number of traces was overall more stable, with only ∼18% loss at the highest threshold level. The number of total detected particles, on the other hand, showed a steeper decline. This consequently produced a higher T:P ratio (40% > > 56%), providing more representative results (i.e., estimation of particle size and epitope abundance) with respect to the whole population. However, this also created a bias in the traces, introducing the preference for significantly bigger and brighter particles (Figure 2c). Therefore, in order to acquire more representative data of the whole particle population, the tradeoff needs to be made by excluding smaller and dimmer particles from the analysis. With these experiments, we defined an acceptable T:P ratio to be at least 35%, for both scatter and fluorescence analyses, as it provided the optimal balance between the gain in data reliability and the loss of sensitivity. This strategy was applied and verified in the subsequent experiments with antibody-stained EVs, where the particles were much dimmer and more difficult to trace, compared to the scattering events or commercial FLuoEVs, thus yielding a very low T:P ratio (< 15%). Such conditions urged us to use a variable Minimum Brightness threshold throughout the different measurements, in order to satisfy the acceptance criteria (example with antibody-stained EVs provided in Figure S4). This is likely just the limitation of the current NTA software version. Future updates will probably bring significant improvements to the T:P ratio, even for the dimmest of the events, boosting the instrument's sensitivity, resolution, and analytical reliability.

3.3 | Analysis of size, concentration, and epitope abundance on small and medium-sized EVs

After the initial comparison with synthetic nanoparticles and setting of the standardized protocols for fluorescence measurement expressed in ERF, purified small EVs from the COLO cell line were labelled with antibodies against common EV markers (CD9 or CD63 (Welsh et al., 2024)) and analyzed in both scatter and fluorescence mode on NTA and nFCM. In scatter mode, particle concentration was comparable between the two instruments, while particle size appeared larger on SNTA (Figure 3a). Similar discordance in size estimation between SNTA and nFCM was reported before (Arab et al., 2021; Vogel et al., 2021). The results may vary due to the differences in the way each instrument calculates the particle size. NTA relies on the Brownian motion, while nFCM infers the size from the side scattered light. The latter is calibrated using silica beads, which still have a higher refractive index and scatter more light than EVs of the same size (van der Pol et al., 2021; Varga et al., 2018; Welsh et al., 2023). This might explain the comparable results between SNTA and nFCM for SiNPs in Figure 1, and a slight discrepancy in EV size estimation later on.

With the fluorescence measurements, the concentration of the CD9+ events was similar between the instruments, while CD63+ events were almost 15-fold higher on nFCM (Figure 3b and Supplementary Material 4). The particle size for CD9+

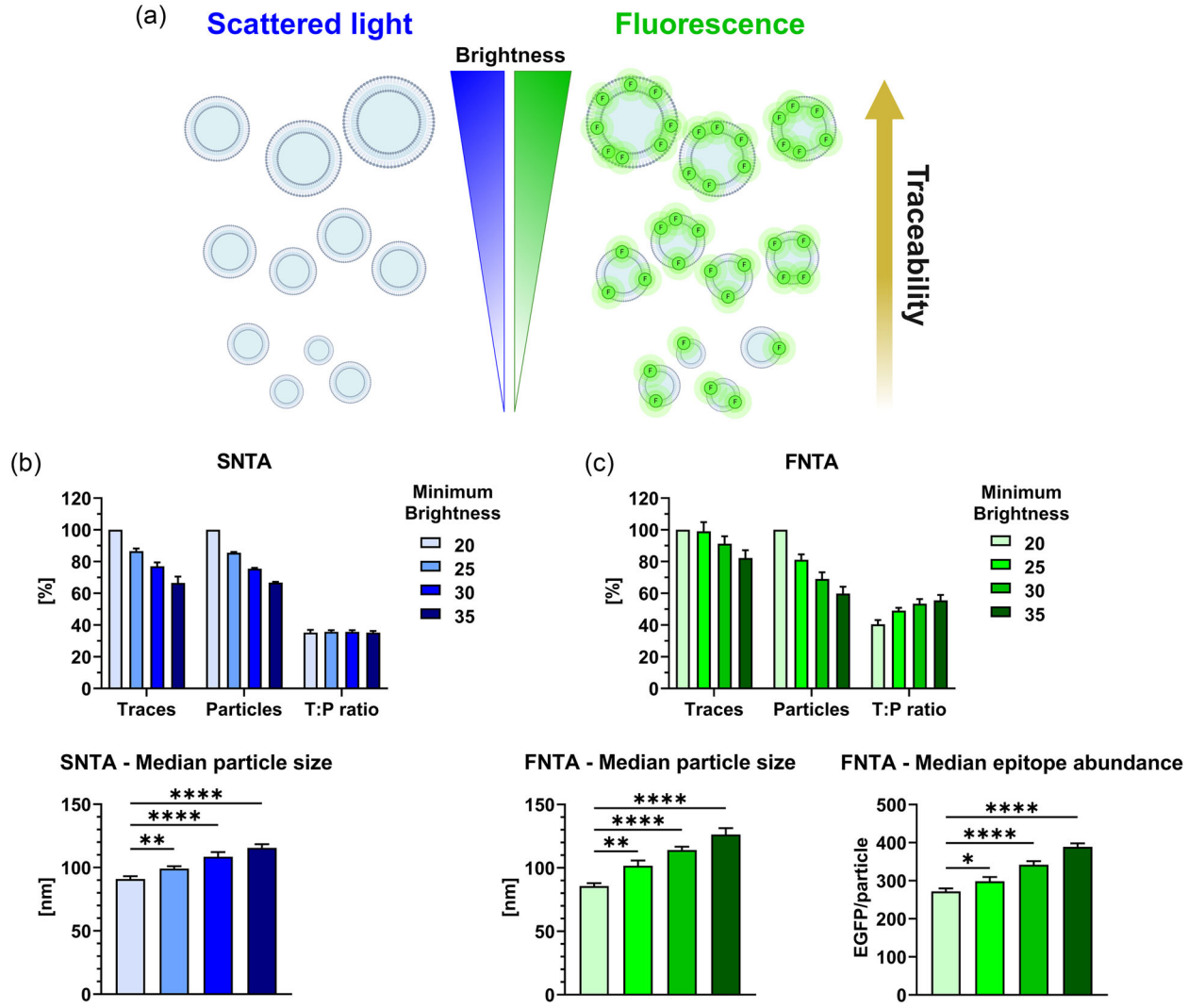

FIGURE 2 Effect of the minimum brightness levels on NTA analyses. (a) NTA's capability to trace a particle depends on the particle's brightness level (scattered light or fluorescence). To assess particles' detectability and traceability in different brightness threshold levels, commercially available FLuoEVs (CD63-EGFP) were analyzed on NTA in both scatter and fluorescence mode (SNTA and FNTA). (b) By increasing the post-acquisition parameter in SNTA, which defined minimum brightness of statistically relevant events, the number of detected particles and traces decreased, as expected. Nevertheless, the T:P ratio remained unchanged (~35%), which means that the analyses kept the same level of representativeness for the detected particles. However, the traced particles were significantly larger in size at the higher threshold levels. (c) In FNTA analyses, increasing the minimum brightness had a similar negative effect on the number of total detected particles. However, the number of traces did not change drastically. Thus, the T:P ratio improved, providing more representative analysis amongst the total detected particles. The tradeoff was that both the median particle size and epitope abundance significantly increased with each increment in threshold level. Statistical significance was analyzed using ordinary one-way ANOVA with Dunnett's test for multiple comparisons (alpha = 0.05, $p = 0.1234$ [ns], 0.0332 [*], 0.0021 [**], 0.0002 [***], < 0.0001 [****]). The graphic was created with Biorender. FNTA, fluorescent NTA; NTA, nanoparticle tracking analysis; SNTA, NTA in scatter mode.

events was comparable to the data obtained in scatter mode, however, the CD63+ events appeared larger, especially on FNTA (Figures 3b, S5 and S6, and Supplementary Material 4). Epitope abundance per single EV was estimated based on the linear regression equation obtained with FS beads and their respective ERF assignments, as described in Materials and Methods. The average (and median) number of anti-CD9 antibodies bound per EV was 2.4 times (and 3.6 times) higher on nFCM than FNTA–287 versus 121 (median 153 vs. 42) antibodies/particle, respectively. At the same time, when analyzing CD63+ events, nFCM was able to detect more particles with much lower average (and median) epitope abundance than FNTA–18 versus 46 (median 11 vs. 21) antibodies/particle, respectively. The increased brightness threshold for FNTA CD63 analyses, necessary to meet the T:P ratio criteria (see Materials and Methods), partly contributed to this outcome by limiting the analyses to mostly bigger particles displaying more epitopes (Figure 3b). Contrary to CD9, CD63+ events appeared to have more homogeneous epitope stoichiometry, evidenced by the absence of extremely bright events in the whole population and a very low average antibodies/particle (closer to the median). The same samples were analyzed also with a plate reader (Figure 3c and Supplementary Material 4), and the

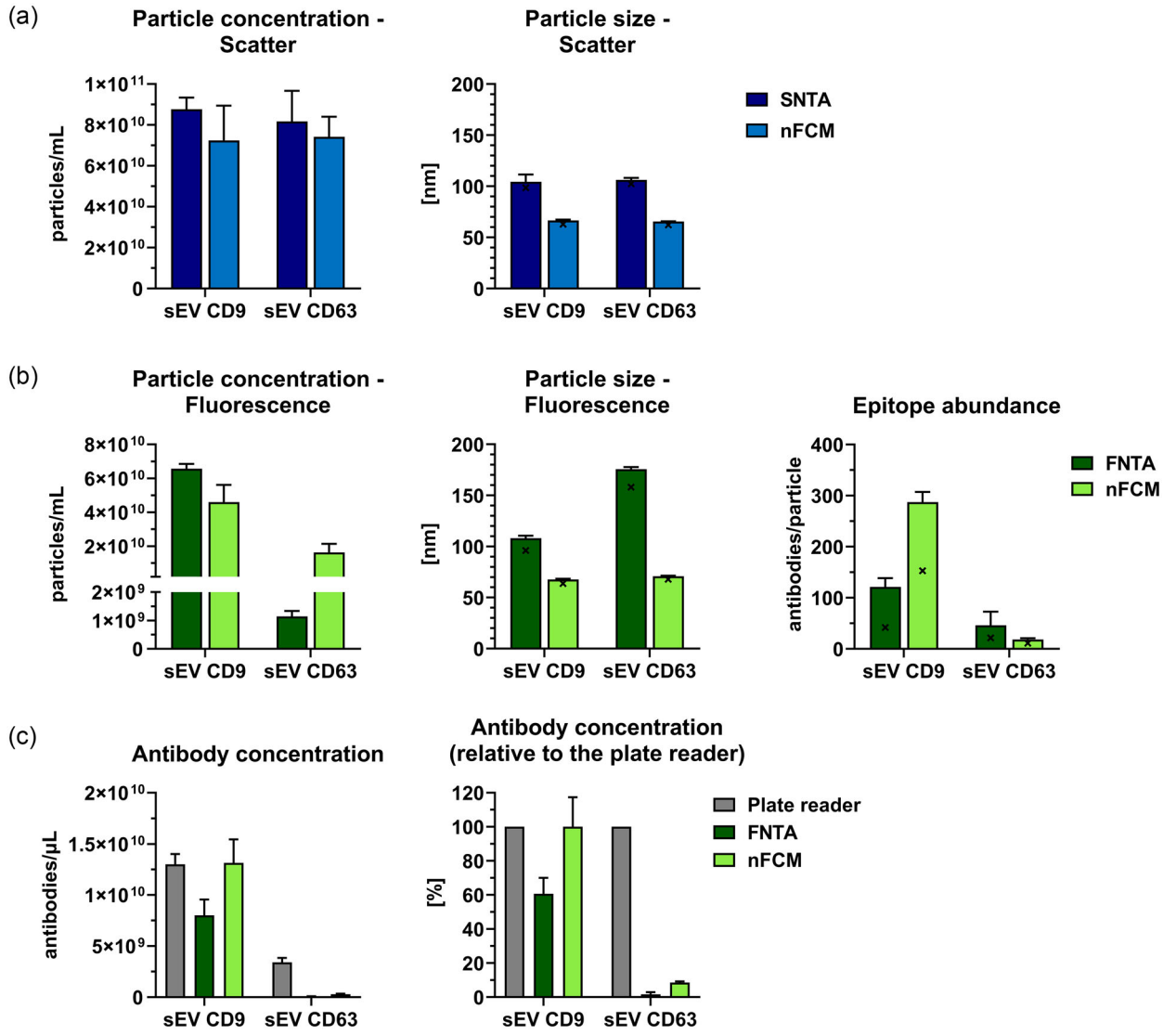

FIGURE 3 COLO sEVs labeled with anti-CD9 and anti-CD63 antibodies. COLO sEVs labeled with anti-CD9-AF488 and anti-CD63-AF488 were analyzed in both (a) scatter and (b) fluorescence mode on NTA and nFCM. Particle size is showing the average and median (bar and 'x' symbol). Average and median (bar and 'x' symbol) epitope abundance per particle were estimated using a linear regression formula plotted with the FS beads assigned with each antibody separately (Supplementary Materials 1, 2, and 3). (c) Antibody concentration per volume of sample was calculated from the average epitope abundance and the fluorescent particle concentration, and compared to the bulk fluorescence measurement performed in the plate reader. Data are shown as the mean ± SD of at least three independent experiments. Representative PSD histograms and dot plots are shown in Figures S5 and S6. NTA, nanoparticle tracking analysis; PSD, particle size distribution.

overall antibody concentration was calculated as described in Materials and Methods (subchapter Microplate reader). This bulk measurement was compared with FNTA and nFCM readouts, and it showed that the latter enabled more accurate estimation of EV-bound anti-CD9 antibody concentration. The reason for such difference between FNTA and nFCM antibody concentration estimates, in spite of comparable particle concentrations, was assumed to be sampling and analysis bias towards brighter particles. To confirm this hypothesis, we applied a more restrictive gating in the nFCM dot plot analyses by limiting the acceptance criteria and excluding the top 1% or 5% of the brightest events, according to their fluorescence intensity on the Y axis of the bivariate plot. This in turn reduced the estimated total antibody concentration by 18% and 37%, respectively, making the latter analysis more aligned with FNTA estimates (Figure S7). These observations highlighted the significance of the gating strategy and the impact it had on the final results. On the other hand, concentration of anti-CD63 antibodies in the sample was greatly underestimated by both nFCM and FNTA (Figure 3c and Supplementary Material 4). This meant that most of the CD63+ events were still under the limit of detection (LoD), due to the low CD63 antigen expression per single small EV. Similar observations were made in a previous study in which Western blot bulk analyses showed higher CD63 marker expression in plasma EVs purified by SEC, even though single particle measurements indicated otherwise (Tian et al., 2020). As previously reported, the overall detectability of

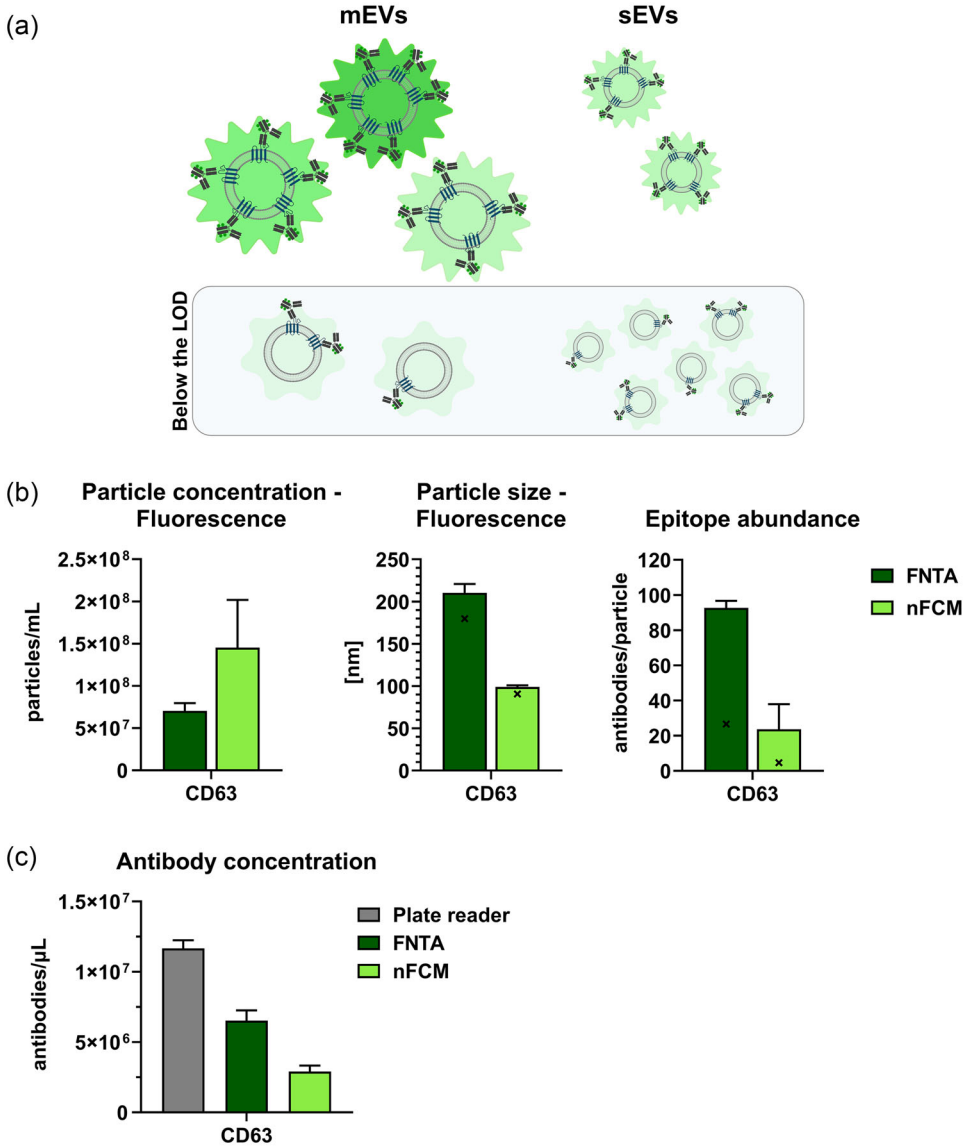

FIGURE 4 COLO mEVs labeled with anti-CD63 antibodies. (a) By increasing the particle size, the CD63 epitope abundance would increase as well, raising the events' brightness above the LoD, and enabling more reliable and inclusive single particle analyses than with sEVs. (b) COLO mEVs labeled with anti-CD63-AF488 were analyzed on FNTA and nFCM. Particle size is showing the average and median (bar and 'x' symbol). Average and median (bar and 'x' symbol) epitope abundance per particle were estimated using a linear regression formula plotted with the FS beads assigned with the anti-CD63 antibody (Supplementary Materials 1, 2, and 3). (c) Antibody concentration per volume of sample was calculated from the average epitope abundance and the fluorescent particle concentration, and compared to the bulk fluorescence measurement performed in the plate reader. Data is shown as the mean ± SD of at least three independent experiments. Representative PSD histograms and dot plots are shown in Figures S8. Graphic was created with Biorender. nFCM, nano-flow cytometry; FNTA, fluorescent NTA; PSD, particle size distribution.

the signal is also affected by the fluorophore brightness and F:P ratio of the antibody used (Weiss et al., 2024). Considering that AF488 is much dimmer than some alternative fluorophores, for example, PE (~24x brighter than AF488), even the high F:P ratio might not be enough for successful detection of particles like CD63+ COLO sEVs.

Altogether, these results highlight the importance of gating strategy, epitope abundance, fluorophore brightness, and F:P ratio for the inclusion or exclusion of certain fluorescent events from the analysis, thus affecting the total antibody detection by FNTA or nFCM. In such a scenario, bulk measurement of the total antibody signal with a plate reader can serve as a good normalizer and help evaluate how representative the single-EV characterization methods are.

We hypothesized that by increasing the particle size, the CD63 epitope abundance would increase as well, raising the events' brightness above the LoD, and enabling more reliable and inclusive single-particle analyses than with sEVs (Figure 4a). To test this hypothesis, we analyzed medium-size-EV (mEVs > 150 nm) enriched samples from the COLO cell line labelled with the same anti-CD63 antibody. When comparing the fluorescence analyses between the FNTA and nFCM, the results were relatively

in line with the initial observations made with CD63+ sEVs. With nFCM, we detected more particles with lower epitope abundance, while FNTA measured mostly larger particles with higher epitope abundance (Figure 4b). This time, the discrepancy in particle concentration between the FNTA and nFCM was not as prominent as before (~2-fold with CD63+ mEVs vs. ~15-fold with CD63+ sEVs), indicating that the events became bright enough for improved FNTA detection. The apparent particle size was unexpectedly small on nFCM (average of ~100 nm) (Figures 4b and S8, and Supplementary Material 4). To a certain degree, we can suspect that some of the detected particles were indeed smaller, as mEVs-enriched samples may still contain also sEVs, causing the shift in the size estimate. On the other hand, we acknowledged that using silica beads as a reference material for EV size calibration may be suboptimal. The average epitope abundance was now increased, compared to the CD63+ sEVs (93 antibodies/particle for FNTA and 24 antibodies/particle for nFCM), and the overall estimated antibody concentration in the sample drastically improved (Figure 4c). Similar to CD9+ sEVs before, we observed that the unbalanced CD63 epitope stoichiometry in mEVs now created an analytical bias—the fewer brightest events, carrying the majority of antibodies, skewed the antibody concentration results, this time in favour of FNTA, even though nFCM demonstrated higher sensitivity by detecting more particles. Nevertheless, it was still evident that plenty of antibodies were left undetected on both instruments. At least in part this could be attributed to the unbound and unwashed antibodies that were not detected in single particle measurements, but were still present in bulk analyses, despite the intensive washing steps. Even with this persisting limitation, we were able to prove our hypothesis that larger particles facilitate the detection of underexpressed markers. Detailed results can be found in the Supplementary Material 4.

3.4 | Estimation of epitope abundance on the small EVs from complex biofluid samples

We proceeded with our experiments by analyzing more complex samples—EVs purified from plasma using SEC. The particles in such a sample display great heterogeneity due to the presence of EVs from multiple cell and tissue sources, as well as the abundance of larger lipoproteins (LPs) that co-elute with EVs. We targeted CD9 and CD63 to assess the broad range of EVs amongst the total EV and non-EV particles, while CD41 and glycophorin A (GYPA) were meant for detection of two most abundant subpopulations derived from platelets and red blood cells, respectively. As expected from such a polydisperse sample, we once again saw the higher particle concentration on SNTA compared to nFCM (Figure 5a). The fluorescence analyses proved to be much more challenging with this sample as the LPs:EVs ratio was in favor of the former, yielding an extremely low number of events labeled with antibodies against general or blood-lineage specific markers (Auber & Svenningsen, 2022; Johnsen et al., 2019; Simonsen, 2017). Still, nFCM was able to detect 2–13 times more particles, which were smaller and expressed fewer epitopes per single particle. Our measurements are in line with the distribution of EVs in plasma that is reported to be tilted towards small, nanosized vesicles (Nieuwland et al., 2023) (Figures 5b, S9, S10). The lowest epitope abundance measured on nFCM was for GYPA+ EVs, with an average of 11 (median of 5) antibodies/particle. The highest average epitope abundance measured on nFCM was with CD41, at 130 antibodies/particle, while the highest median epitope abundance was detected with CD63, showing 17 antibodies/particle (Figure 5b and Supplementary Material 4). In fact, we found that the CD9 and CD63 average epitope abundance estimations made with nFCM, were in fine agreement with earlier studies performed with qSMLM (Saftics et al., 2023). The concordance extended also to the measured average particle size, even if slightly smaller on nFCM. The reason for measuring apparently smaller size on nFCM than qSMLM is likely the same as mentioned before, that is, due to the usage of silica beads as a reference material for the scattering profile of EVs.

Due to the lower sensitivity of the FNTA, the majority of detected particles were larger EVs with higher epitope abundance (Figures 5b, S9 and S10). FNTA struggled to detect and maintain the trace length for many of the events throughout the acquisition, requiring a higher Minimal Brightness threshold in order to maintain T:P ratio ≥35%, comparable to the scatter measurements (see Materials and Methods). As a result, particles included in the statistical analyses were much larger and brighter but still maintained a similar marker expression trend as observed with nFCM—the lowest was GYPA, with an average of 245 (median of 61) antibodies/particle, and the highest was CD63, with an average of 574 (median of 140) antibodies/particle. For most of the analyzed samples, both FNTA and nFCM detected 5%–20% of the total antibodies compared to the bulk plate reader estimates (Figure 5c and Supplementary Material 4). However, with the FNTA's biased analyses of mostly brighter events, the estimated antibody concentration was much higher in the case of CD9 and CD41 markers, reaching more than 60% of the bulk estimates. Once more, we observed that the biased analysis and a non-Gaussian distribution of certain epitopes are the main reasons for such highly concordant results between FNTA single particle analysis and microplate reader bulk measurements. With the exclusion of just 1% or 5% of the top brightest events, the number of detected antibodies in FNTA decreased by 22% or 36%, respectively (Figure S11).

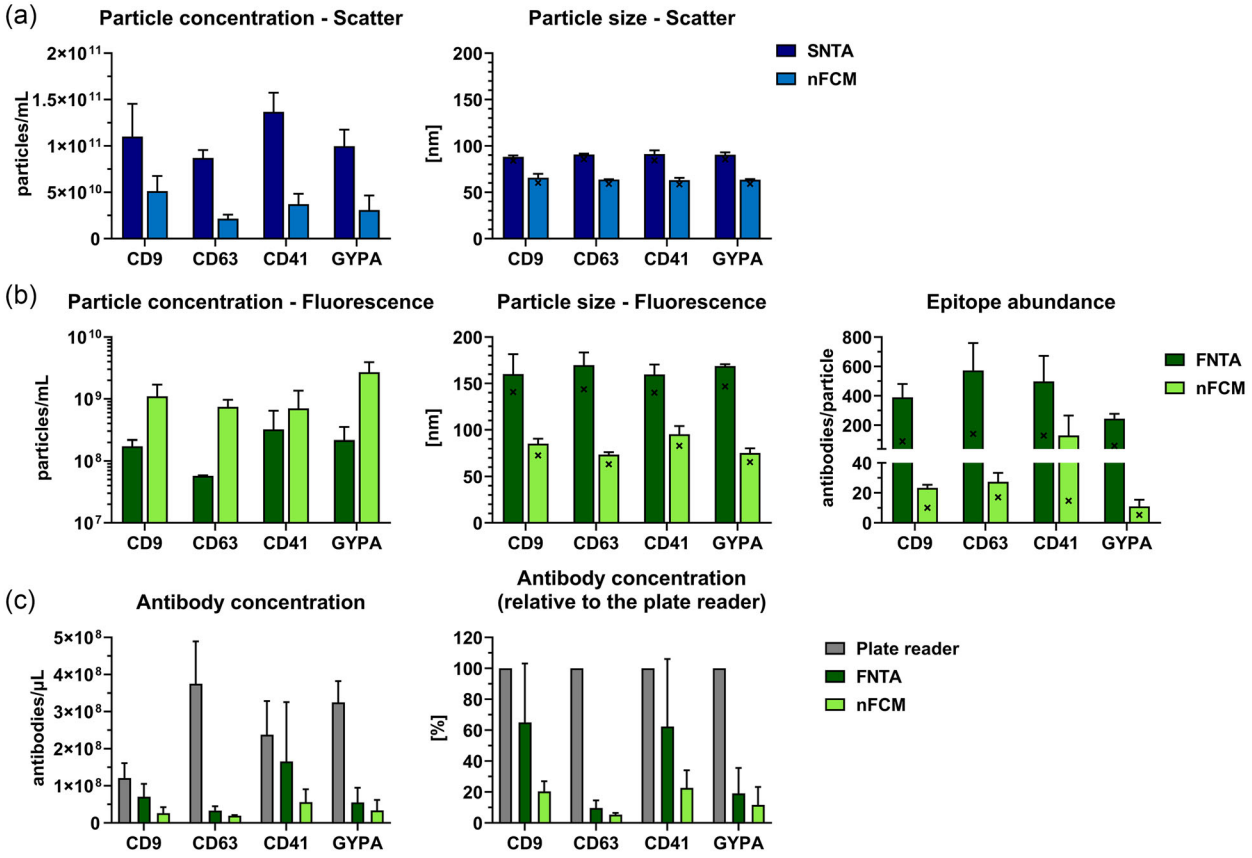

FIGURE 5 Plasma EVs labeled with antibodies against general and blood-lineage specific markers. SEC-purified plasma EVs labeled with anti-CD9, anti-CD63, anti-CD41, and anti-GYPA antibodies (AF488 conjugates) were analyzed in both (a) scatter and (b) fluorescence mode on NTA and nFCM. Note the $\log_{10}$ scale for the fluorescent particle concentration. Particle size is showing the average and median (bar and 'x' symbol). Average and median (bar and 'x' symbol) epitope abundance per particle were estimated using linear regression formula plotted with the FS beads assigned with each antibody separately (Supplementary Materials 1, 2, and 3). (c) Antibody concentration per volume of sample was calculated from the average epitope abundance and the fluorescent particle concentration, and compared to the bulk fluorescence measurement performed in the plate reader. Data are shown as the mean ± SD of at least three independent experiments. Representative PSD histograms and dot plots are shown in Figures S9 and S10. AF488, Alexa Fluor 488; EV, extracellular vesicles; GYPA, glycophorin A; nFCM, nano-flow cytometry; NTA, nanoparticle tracking analysis; SEC, size exclusion chromatography

3.5 | Approximating the instruments' sensitivity levels

Since nFCM produced better linearity and resolution than FNTA for fluorescence analyses, we provided the overview of their respective accuracies (portrayed in residual plots) and approximated their sensitivity levels. Using the F:P ratio of multiple antibodies (information provided by the manufacturer, Supplementary Material 1), and appropriate correction factors (as described in Materials and Methods and Supplementary Material 2), we converted ERF of FS beads from antibodies/bead to AF488/bead. The linear regression was then plotted using measured MFI values and assigned AF488 values of FS beads (log-transformed), and the equations were used to back-calculate the AF488/bead (Figure 6). The following formula was used to calculate the residuals (the difference between the actual value and the value predicted by the linear regression model) for both FNTA and nFCM: $\frac{|[Assigned\ AF488]-[Calculated\ AF488]|}{[Assigned\ AF488]}$%. Due to the apparently poor detection of the dimmest FS beads, the residuals were quite high in the lower ranges, more so for FNTA than for nFCM. Based on this, we used FS20 beads as our reference for the lowest quantifiable MFI on both instruments. We then introduced 'assumed AF488/bead' as a hypothetical value that would ensure better linearity (with residuals < 15%) for the same measured MFI. This value served as an approximation of instruments' sensitivity levels, estimated at ~115 AF488 molecules for FNTA and ~75 AF488 molecules for nFCM (Figure 6a,b). This further translates to ~25 and ~16 antibodies per particle, respectively, although, subjected to a high variation depending on the individual antibody's F:P ratio. For example, anti-GYPA-AF488 antibody, with the F:P = 5, provided better detection of dimmer events, than anti-CD41-AF488, with F:P = 2.9 (Figure 5b, Supplementary Material 1). Alternatively, the LoD can be calculated based on the calibration curve according to a standard formula (Borman & Elder, 2017): $= 3.3 \times \frac{\sigma}{S}$. The standard error of the response is represented by σ, while S is the slope of the calibration curve. This translates to LoD of 21 AF488 molecules for FNTA and 9 AF488 molecules

(a)

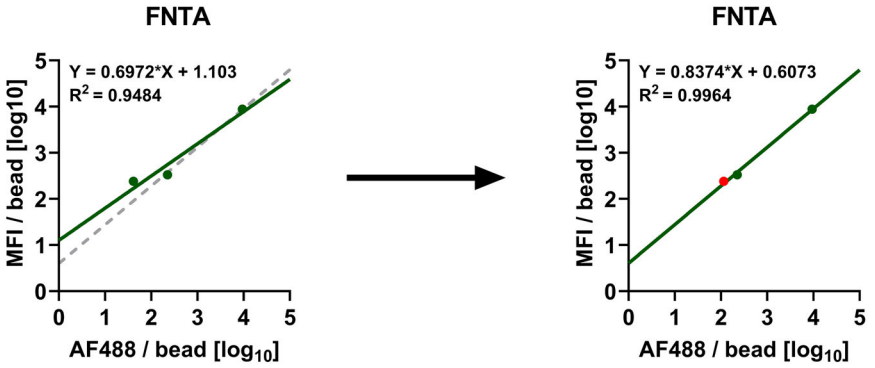

FNTA			
Fluospheres	Assigned AF488	Calculated AF488	Residuals
20 nm	41	68	65%
40 nm	225	108	52%
100 nm	9406	11824	26%

FNTA (target residuals <15%)			
Fluospheres	Assumed AF488	Calculated AF488	Residuals
20 nm	115	131	14%
40 nm	225	193	14%
100 nm	9406	9627	2%

(b)

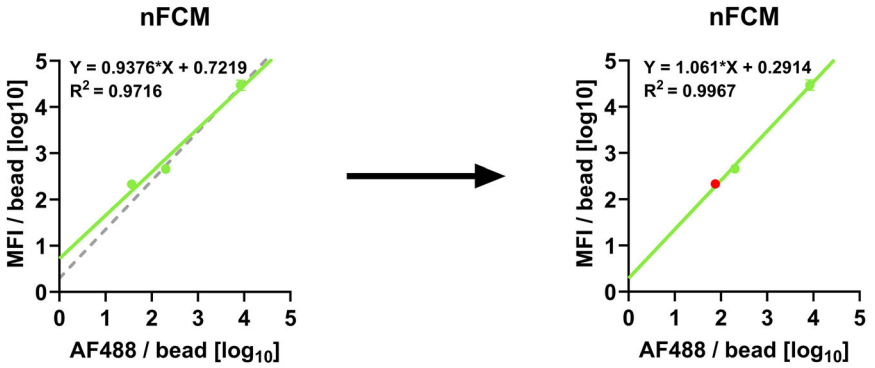

nFCM			
Fluospheres	Assigned AF488	Calculated AF488	Residuals
20 nm	37	53	45%
40 nm	200	117	42%
100 nm	8370	9902	18%

nFCM (target residuals <15%)			
Fluospheres	Assumed AF488	Calculated AF488	Residuals
20 nm	75	85	13%
40 nm	200	171	14%
100 nm	8370	8646	3%

(c)

$$LoD = 3.3 \times \frac{\sigma}{S}$$

	FNTA	nFCM
Standard error (σ)	0.277	0.938
Slope (S)	0.697	0.274
LoD AF488 [log10]	1.313	0.965
LoD AF488	**21**	**9**

FIGURE 6 Approximation of the analytical sensitivity of FNTA and nFCM. Due to the lack of sensitivity, the linearity was reduced in the lowest ranges of the MFI signal. The grey dotted lines represent the optimal linear regression model, to which the lowest hypothetical FS20 values (marked in red) were fitted to produce more accurate results (residuals < 15%). These values, taken as approximate analytical sensitivity levels, were (a) ~115 AF488 molecules for FNTA and (b) ~75 AF488 molecules for nFCM. (c) Alternatively, the LoD can be calculated as 21 AF488 molecules for FNTA and 9 AF488 molecules for nFCM, by following a standardized formula based on the standard error and slope of the calibration curve. AF488, Alexa Fluor 488; LoD, limits of detection; MFI, median fluorescence intensity; nFCM, nano-flow cytometry; FNTA, fluorescent NTA;

for nFCM (Figure 6c). Indeed, in most of the measurements, the LoD reached levels as low as a couple of antibodies. Novel and more refined standards are still required for a more precise and accurate determination of analytical sensitivity.

4 | DISCUSSION

In this work, we have compared two single particle analysis platforms which are commonly used for EV analysis—NTA and nFCM. We evaluated their performance in both scatter and fluorescence mode using synthetic nanoparticles (silica and fluorescent polystyrene beads of different sizes and fluorescence intensities), and EVs from simple (cell culture media) and complex biofluids (human blood plasma).

We observed that nFCM measurements of polydisperse samples were more in line with the expected values (according to the polydisperse silica beads mix) since larger events might have caused the overestimation of NTA, as reported earlier (Vogel et al., 2021). We acknowledge that this was likely a limitation of using a single instrument setting on NTA for analyzing a wide range of particles in our experiments. Furthermore, in most of the EV measurements, NTA reported a larger particle size compared to nFCM. To some degree, this can be caused by the intrinsic differences in the way these instruments perform size measurements—NTA calculates the particle size from the Brownian motion, while nFCM relies on the particle's refractive index and side scattering light. The latter is calibrated using silica beads as a reference material, which introduces a level of uncertainty because solid silica beads scatter more light than EVs (van der Pol et al., 2021; Varga et al., 2018). The disparity between NTA and nFCM size measurements was even more pronounced in fluorescence mode since FNTA biased larger EVs with concomitantly higher marker abundance.

In fluorescence mode, both instruments were struggling to detect the dimmest events, although nFCM was more sensitive, as demonstrated by greater linearity and resolution produced with FS beads of three different levels of fluorescence intensity (Figures 1 and 6). The residuals in lower ranges were still substantial as we were operating on the very limit of detection for both instruments. Nevertheless, our method still enables a higher level of quantification, standardization, and cross-platform comparability than the relative fluorescence units, or simple digital quantification (positive vs. negative particles in fluorescence measurement). In fact, the level of accuracy of our standardization approach seems to outperform current state-of-the-art calibration techniques with conventional flow cytometry MESF calibrators (Lozano-Andrés et al., 2024). The recent work of Lozano-Andrés et al. showed that despite the high linearity and complementarity between different batches of beads for a similar quantitative range, these calibrators still failed to project a comparable level of accuracy and confidence in the fluorescence range of EVs. Reported variation in MESF estimates, based on the used flow cytometry calibrators, reached 157% for EVs stained with anti-CD9-PE while analyzing true residuals in the EV range was virtually impossible since it was at least two orders of magnitude below the quantification range of the beads. Having a fluorophore that is ~24× brighter than AF488 (brightness of PE = 1,607,200 M^{-1} cm^{-1} vs. AF488 = 67,160 M^{-1} cm^{-1}), did not seem to help in mitigating the circumstances. All of the aforementioned observations demonstrate the limitations of using big and bright beads from flow cytometry to extrapolate and calibrate the low levels of fluorescence intensities of EVs. Together with the fact that the flow cytometry beads are incompatible with instruments such as FNTA and nFCM, this makes a compelling argument for the adoption of our fluorescence standardization method with FS beads.

Hard-dyed beads are generally not recommended for fluorescence calibration, due to the high spectral mismatching with respect to the fluorophores used to stain EVs (Hoffman et al., 2012; Welsh et al., 2023). However, the yellow-green FS beads show a single-peak emission spectrum, highly concordant with that of AF488, making it a suitable candidate for such application. Standardized production, which ensures a low polydispersity index (6%–14% for FS beads batches used in our experiments), and accurate bead concentration (derived from the dry weight of the beads, the density of polystyrene, and the bead diameter), further supports the suitability of FS beads for ERF assignment. Indeed, a similar strategy was reported before, using soluble AF488 and yellow-green FS beads for ERF assignment (Chen et al., 2015; Gao et al., 2021).

With the described methodology we were also able to approximate the instruments' sensitivity levels and calculate the LoD of 21 and 9 AF488 molecules for FNTA and nFCM, respectively. Even with such respectable sensitivity levels, we observed that many fluorescent events went undetected (by comparing FNTA, nFCM, and plate reader data). We cannot entirely rule out that some of the signal detected by the plate reader originated from the unbound antibodies that might have remained in the sample even after rigorous washing, although our dye+PBS controls showed complete antibody removal (data not shown). Apart from that, the lack of detection of many fluorescent events by FNTA and nFCM was likely influenced by the low epitope abundance per single EV, as well as the fluorophore brightness and F:P ratio of the antibody. Similar observations were made in previous works (Weiss et al., 2024; Welsh et al., 2023). In addition to the sensitivity limitations that can create a bias towards brighter particles, gating strategy appeared also as a factor that can have a considerable impact on the overall analyses. We further exemplified the interplay of these variables in FNTA and nFCM analyses in Figure S12. The final result, comparing single particle analyses and bulk measurements, was particularly affected by the level of inclusiveness of the brightest events, which hauled majority of the bound antibodies (demonstrated also in the Figures S7 and S11). By focusing only on the small number of the brightest events, we were able to detect most of the bound antibodies in the sample, and acquire results that had highest complementarity with the data of the

plate reader bulk analyses. Such analytical paradox may instigate the polemics regarding the race for development, and finally utility, of the most sensitive instrument for EV analyses. The argument in favour would be that the higher sensitivity conveys more informative assessment of EVs, with insights into their true heterogeneity and marker stoichiometry. High sensitivity capabilities are particularly advantageous for diagnostic application of EVs where the abundance of a disease biomarker per single EV can be lower (e.g., 16 CA19-9 molecules/EV in cancer patients vs. 31 in healthy individuals) (Lennon et al., 2019). In this case, EV analytical instruments lacking sensitivity would not be able to detect the tumour-derived EVs.

Our analyses bring into perspective the dynamic expression and distribution of different EV markers, raising interesting points on plasma EV biology. Thus, we further compared the scientific consensus in the literature with our observations of the total plasma EV concentration and the subpopulation heterogeneity. By looking at the average positivity for all of the markers and normalizing it per volume of input biofluid, we assessed the EV concentration with FNTA to be ~1.9×10^9 EVs/mL of plasma, while with nFCM it was ~1.4×10^{10} EVs/mL of plasma, which was more in line with the expected estimates of ~2×10^{10} EVs/mL of healthy-donor plasma (Auber & Svenningsen, 2022; Johnsen et al., 2019). Of course, we also keep in consideration that SEC was used for EV isolation from plasma before analysis and that the recovery of EVs from a complex fluid can have variable efficiency which is also dependent on the donor sample variability. Similar to the previous report (Tian et al., 2020), we observed with nFCM that the red blood cell (RBC)-derived EVs (GYPA+) were more abundant than those from platelets (CD41+), which was further corroborated with a bulk ELISA assay (Figure S13). This may appear somewhat conflicting, since some other studies, as well as our FNTA results, indicate otherwise (Auber & Svenningsen, 2022; Gąsecka et al., 2021; Karimi et al., 2022; Nieuwland & Siljander, 2024; Palviainen et al., 2020). In certain instances, such a discrepancy could be explained by the extent of platelet activation in different experiments, which could create EV artefacts if the pre-cleared plasma still has some remaining platelets, or if the serum is used instead. On the other side, from a physiological point of view, EV-mediated material removal is suggested to be implicated in a reticulocyte-to-erythrocyte maturation (Johnstone et al., 1987), the continuous and high-turnover process, making the predominance of GYPA+ vesicles in human blood plausible. Another point of view would be that the stoichiometry and epitope abundance were not considered in the previous studies, leading to the conclusion that platelet EVs make up the majority, while in fact, most of the RBC EVs are just undetectable, due to the low epitope abundance per single particle and the lacking analytical sensitivity, as discussed before. This presumption is well in agreement with the provided example, in which an Apogee A60 instrument, calibrated for the measurement of EVs in the size range of 160–1000 nm, was used for the analyses of platelet- and RBC-derived EVs in plasma (Nieuwland & Siljander, 2024). Even though the measured relative proportion of these subpopulations is comparable to what we observed with FNTA (more platelet EVs than RBC EVs), their actual concentration appears to be ~50× and ~100× lower than FNTA estimates (or ~130× and ~1300× lower than nFCM estimates), respectively. This suggests that the vast majority of plasma EVs were likely undetected within such a high calibration range (160–1000 nm). Furthermore, RBC EVs were probably more affected in the analysis, due to the much lower GYPA abundance per single EV. In that case, it is not a surprise that with progression in the sensitivity from lower to higher (Apogee A60 < FNTA ZetaView < nFCM NanoAnalyzer), not only that we see the change in the concentration of detected EVs, but also the change in the subpopulation proportions, that is, RBC EVs becoming more abundant than platelet EVs.

Looking into the expression of the CD41 and GYPA markers on a cellular level, we can divulge and debate the non-randomness of molecular sorting during the EV biogenesis, which creates the suboptimal marker stoichiometry for EV detection. Apparently, one platelet of ~2.5 μm has ~40,000 CD41 molecules on its surface (Nolan & Jones, 2017), while an average-sized RBC can display up to 1,000,000 GYPA copies (Alenghat & Golan, 2013; Dean, 2005). This translates to an epitope density of approximately 1 CD41 molecule per 490 nm^2 and 1 GYPA molecule per 134 nm^2 (Houchin et al., 1958). One could then justifiably expect that the GYPA expression would be almost 4x higher than CD41, per single EV of the same size. Yet, measurements show quite the opposite. The results of nFCM analyses show that CD41+ EVs have similar epitope density as their parental cells (~1 molecule per 445 nm^2; based on the average epitope abundance and average fluorescent particle size), while GYPA+ EVs with 1 molecule per 1749 nm^2 demonstrate considerably lower epitope density compared to their cell of origin. This may suggest the existence of an apparently non-stochastic process, with high level of order in cellular EV packing machinery, which leads to preferential depletion of GYPA from RBC EVs. On the opposite side, CD41 in platelet EVs appears to follow no particular sorting instructions. It is also plausible that sEVs detected in our study originate both from endosomal compartments and from plasma membrane budding of their parent cells. Two biogenesis pathways can result in distinct molecular composition of vesicles and may also be unequally favoured in different cell types. For instance, platelets are reported to produce ectosomes (membrane originated) and exosomes (of endosomal origin), both displaying platelet antigens, but only latter being enriched in CD63 (Heijnen et al., 1999; Karimi et al., 2022). In reticulocytes, instead, the selective removal of proteins and enzymes during the erythrocyte formation is predominantly occurring through exosomes (Johnstone et al., 1989), possibly explaining their different membrane composition with respect to that of the parent cell. Of course, we have to make our interpretations cautiously due to some procedural and instrumental factors that might influence the epitope (and epitope density) readout, such as antibody's affinity and avidity, or instrument's inability to detect all of the EVs, hence, providing biased results. In spite of these limitations that could restrict direct comparison of EV and cellular epitope densities, certain relative comparisons could still be made amongst EVs alone. Deeper analyses of individual EVs (using FCS files) might reveal stoichiometric subpopulations within subpopulations, that is, groups of EVs expressing the same marker but with different epitope densities. For example, looking at the CD9+ COLO

sEVs on FNTA in the size range 40–100 nm and 100–200 nm, we could see that the smaller subpopulation has on average 100 antibodies/particle with epitope density of ~570 nm^2, while the larger subpopulation had an average of 135 antibodies/particle and density of ~1500 nm^2. Similar analyses were achieved with qSMLM and EVs from pancreatic cancer patients, revealing that disease-associated EVs had drastically lower epitope density (Lennon et al., 2019). This demonstrates that our methodology enables more insightful analyses of plasma EVs by bringing into perspective the dynamic expression and distribution of different EV markers, transcending a simple semiquantitative profiling using FNTA and nFCM. Furthermore, this kind of multiparametric analyses and information can feed the future in silico models, which could aid in EV analytics, boost the EV biomarker discovery and validation, and facilitate the development of EV-based liquid biopsies.

5 | CONCLUSIONS

Our study introduces a method for standardizing fluorescence quantification and facilitating comparison across different single-particle analysis instruments, such as FNTA and nFCM. As such, it represents a first-of-a-kind protocol which allows quantitative fluorescence measurements using FNTA. This approach enables a deeper characterization of EV subpopulations and a better understanding of analytical capabilities.

We further highlight the significance of the instrument's gating strategy and sensitivity, together with epitope abundance, fluorophore brightness, and antibody's F:P ratio, in shaping the final result of single-EV analyses. We propose in-parallel bulk fluorescence measurements as a reliable tool for assessing markers that are below the detection limit of single-particle analysis instruments and for normalizing the data.

We also evidence the opportunity and feasibility of gating strategies and software adjustments to boost and balance the instrument sensitivity and analytical reliability, both paving the way towards more robust EV biomarker detection.

Overall, our work provides a valuable contribution to the ongoing development and optimization of EV analytical platforms and future EV diagnostic tools.

AUTHOR CONTRIBUTIONS

Danilo Mladenović: Conceptualization (equal); data curation (equal); formal analysis (equal); funding acquisition (supporting); investigation (equal); methodology (equal); project administration (equal); resources (supporting); validation (equal); visualization (equal); writing — original draft (equal); writing — review and editing (equal). **Joseph Brealey**: Data curation (equal); formal analysis (equal); investigation (equal); methodology (equal); resources (equal); validation (equal); visualization (equal); writing — review and editing (equal). **Ben Peacock**: Data curation (equal); formal analysis (equal); investigation (equal); methodology (equal); resources (equal); validation (equal); visualization (equal); writing — review and editing (equal). **Kairi Koort**: Funding acquisition (supporting); resources (equal); supervision (supporting); writing — review and editing (equal). **Nataša Zarovni**: Conceptualization (equal); funding acquisition (lead); project administration (equal); resources (equal); supervision (lead); writing - original draft (equal); writing — review & editing (equal).

ACKNOWLEDGEMENTS

This work was supported by the following funding programs: Tallinn University Research Fund (project number TF7320); European Regional Development Fund Enterprise Estonia's Applied Research Program under the grant agreement number 2014–2020.4.02.21-0398 (EVREM); Estonian Research Council, Research Infrastructures of National Importance TT11 (ELIXIR).

CONFLICT OF INTEREST STATEMENT

D.M. is an Applied Scientist in the company HansaBioMed Life Sciences, which is the manufacturer of the products (PURE-EVs, FLuoEVs, lyophilized exosomes and microvesicles standards, ExoTEST ELISA kits) used in this study. J.B. is a Junior Researcher and B.P. is the Head of Research in the company NanoFCM, which is the manufacturer of the NanoAnalyzer U30 instrument used in this study.

ORCID

Danilo Mladenović https://orcid.org/0000-0002-0877-2035
Joseph Brealey https://orcid.org/0000-0002-3013-9375
Ben Peacock https://orcid.org/0000-0002-7823-8719

REFERENCES

Alenghat, F. J., & Golan, D. E. (2013). Membrane protein dynamics and functional implications in mammalian cells. *Current Topics in Membranes*, *72*, 89–120. https://doi.org/10.1016/B978-0-12-417027-8.00003-9

Arab, T., Mallick, E. R., Huang, Y., Dong, L., Liao, Z., Zhao, Z., Gololobova, O., Smith, B., Haughey, N. J., Pienta, K. J., Slusher, B. S., Tarwater, P. M., Tosar, J. P., Zivkovic, A. M., Vreeland, W. N., Paulaitis, M. E., & Witwer, K. W. (2021). Characterization of extracellular vesicles and synthetic nanoparticles with four orthogonal single-particle analysis platforms. *Journal of Extracellular Vesicles*, *10*(6), e12079. https://doi.org/10.1002/jev2.12079

Auber, M., & Svenningsen, P. (2022). An estimate of extracellular vesicle secretion rates of human blood cells. *Journal of Extracellular Vesicles*, *1*(6), e46. https://doi.org/10.1002/jex2.46

Bagci, C., Bahcekapili, M. S., Belder, N., Bennett, A. P. S., Erdener, S. E., & Dalkara, T. (2022). Overview of extracellular vesicle characterization techniques and introduction to combined reflectance and fluorescence confocal microscopy to distinguish extracellular vesicle subpopulations. *Neurophotonics*, *9*(2), 021903. https://doi.org/10.1117/1.NPh.9.2.021903

Bao, C., Xiang, H., Chen, Q., Zhao, Y., Gao, Q., Huang, F., & Mao, L. (2023). A review of labeling approaches used in small extracellular vesicles tracing and imaging. *International Journal of Nanomedicine*, *18*, 4567–4588. https://doi.org/10.2147/IJN.S416131

Bobrie, A., Colombo, M., Krumeich, S., Raposo, G., & Théry, C. (2012). Diverse subpopulations of vesicles secreted by different intracellular mechanisms are present in exosome preparations obtained by differential ultracentrifugation. *Journal of Extracellular Vesicles*, *1*(1), 18397. https://doi.org/10.3402/jev.v1i0.18397

Borman, P., & Elder, D. (2017). Q2(R1) validation of analytical procedures. In *ICH Quality Guidelines*, (pp. 127–166). John Wiley & Sons, Ltd. https://doi.org/10.1002/9781118971147.ch5

Breitwieser, K., Koch, L. F., Tertel, T., Proestler, E., Burgers, L. D., Lipps, C., Adjaye, J., Fürst, R., Giebel, B., & Saul, M. J. (2022). Detailed characterization of small extracellular vesicles from different cell types based on tetraspanin composition by ExoView R100 platform. *International Journal of Molecular Sciences*, *23*(15), 8544. https://doi.org/10.3390/ijms23158544

Buranda, T., Wu, Y., & Sklar, L. A. (2011). Quantum dots for quantitative flow cytometry. In: Hawley, T., Hawley, R. (eds) Flow Cytometry Protocols. *Methods in Molecular Biology*, *699*, 67–84. https://doi.org/10.1007/978-1-61737-950-5_4

Chen, C., Zhang, X., Zhang, S., Zhu, S., Xu, J., Zheng, Y., Han, J., Zeng, J.-Z., & Yan, X. (2015). Quantification of protein copy number in single mitochondria: The Bcl-2 family proteins. *Biosensors & Bioelectronics*, *74*, 476–482. https://doi.org/10.1016/j.bios.2015.06.057

Choi, D., Montermini, L., Jeong, H., Sharma, S., Meehan, B., & Rak, J. (2019). Mapping subpopulations of cancer cell-derived extracellular vesicles and particles by nano-flow cytometry. *ACS Nano*, *13*(9), 10499–10511. https://doi.org/10.1021/acsnano.9b04480

Cook, S., Tang, V. A., Lannigan, J., Jones, J. C., & Welsh, J. A. (2023). Quantitative flow cytometry enables end-to-end optimization of cross-platform extracellular vesicle studies. *Cell Reports Methods*, *3*(12), 100664. https://doi.org/10.1016/j.crmeth.2023.100664

Dean, L. (2005). *Blood Groups and Red Cell Antigens*. National Center for Biotechnology Information (US).

Filipe, V., Hawe, A., & Jiskoot, W. (2010). Critical evaluation of nanoparticle tracking analysis (NTA) by NanoSight for the measurement of nanoparticles and protein aggregates. *Pharmaceutical Research*, *27*(5), 796–810. https://doi.org/10.1007/s11095-010-0073-2

Fortunato, D., Mladenović, D., Criscuoli, M., Loria, F., Veiman, K.-L., Zocco, D., Koort, K., & Zarovni, N. (2021). Opportunities and pitfalls of fluorescent labeling methodologies for extracellular vesicle profiling on high-resolution single-particle platforms. *International Journal of Molecular Sciences*, *22*(19), 10510. https://doi.org/10.3390/ijms221910510

Gao, K., Zhou, Y., Lu, Q., Lu, J., Su, L., Su, R., Zhang, M., Tian, Y., Wu, L., & Yan, X. (2021). High-throughput human telomere length analysis at the single-chromosome level by fish coupled with nano-flow cytometry. *Analytical Chemistry*, *93*(27), 9531–9540. https://doi.org/10.1021/acs.analchem.1c01544

Gąsecka, A., Pluta, K., Solarska, K., Rydz, B., Eyileten, C., Postula, M., van der Pol, E., Nieuwland, R., Budnik, M., Kochanowski, J., Jaguszewski, M. J., Szarpak, Ł., Mazurek, T., Kapłon-Cieślicka, A., Opolski, G., & Filipiak, K. J. (2021). Plasma concentrations of extracellular vesicles are decreased in patients with post-infarct cardiac remodelling. *Biology*, *10*(2), 97. https://doi.org/10.3390/biology10020097

Görgens, A., Bremer, M., Ferrer-Tur, R., Murke, F., Tertel, T., Horn, P. A., Thalmann, S., Welsh, J. A., Probst, C., Guerin, C., Boulanger, C. M., Jones, J. C., Hanenberg, H., Erdbrügger, U., Lannigan, J., Ricklefs, F. L., El-Andaloussi, S., & Giebel, B. (2019). Optimisation of imaging flow cytometry for the analysis of single extracellular vesicles by using fluorescence-tagged vesicles as biological reference material. *Journal of Extracellular Vesicles*, *8*(1), 1587567. https://doi.org/10.1080/20013078.2019.1587567

Heijnen, H. F. G., Schiel, A. E., Fijnheer, R., Geuze, H. J., & Sixma, J. J. (1999). Activated platelets release two types of membrane vesicles: microvesicles by surface shedding and exosomes derived from exocytosis of multivesicular bodies and alpha-granules. *Blood*, *94*(11), 3791–3799. https://doi.org/10.1182/blood.V94.11.3791

Hendrix, A., Lippens, L., Pinheiro, C., Théry, C., Martin-Jaular, L., Lötvall, J., Lässer, C., Hill, A. F., & Witwer, K. W. (2023). Extracellular vesicle analysis. *Nature Reviews Methods Primer*, *3*, 56. https://doi.org/10.1038/s43586-023-00240-z

Hilton, S. H., & White, I. M. (2021). Advances in the analysis of single extracellular vesicles: A critical review. *Sensors and Actuators Reports*, *3*, 100052. https://doi.org/10.1016/j.snr.2021.100052

Hoffman, R. A., Wang, L., Bigos, M., & Nolan, J. P. (2012). NIST/ISAC standardization study: Variability in assignment of intensity values to fluorescence standard beads and in cross calibration of standard beads to hard dyed beads. *Cytometry Part A*, *81A*(9), 785–796. https://doi.org/10.1002/cyto.a.22086

Houchin, D. N., Munn, J. I., & Parnell, B. L. (1958). A method for the measurement of red cell dimensions and calculation of mean corpuscular volume and surface area. *Blood*, *13*(12), 1185–1191. https://doi.org/10.1182/blood.V13.12.1185.1185

Johnsen, K. B., Gudbergsson, J. M., Andresen, T. L., & Simonsen, J. B. (2019). What is the blood concentration of extracellular vesicles? Implications for the use of extracellular vesicles as blood-borne biomarkers of cancer. *Biochimica et biophysica acta (BBA) - Reviews on Cancer*, *1871*(1), 109–116. https://doi.org/10.1016/j.bbcan.2018.11.006

Johnstone, R. M., Adam, M., Hammond, J. R., Orr, L., & Turbide, C. (1987). Vesicle formation during reticulocyte maturation. association of plasma membrane activities with released vesicles (exosomes). *Journal of Biological Chemistry*, *262*(19), 9412–9420.

Johnstone, R. M., Bianchini, A., & Teng, K. (1989). Reticulocyte maturation and exosome release: transferrin receptor containing exosomes shows multiple plasma membrane functions. *Blood*, *74*(5), 1844–1851. https://doi.org/10.1182/blood.V74.5.1844.1844

Karimi, N., Dalirfardouei, R., Dias, T., Lötvall, J., & Lässer, C. (2022). Tetraspanins distinguish separate extracellular vesicle subpopulations in human serum and plasma—contributions of platelet extracellular vesicles in plasma samples. *Journal of Extracellular Vesicles*, *11*(5), e12213. https://doi.org/10.1002/jev2.12213

Kwon, Y., & Park, J. (2022). Methods to analyze extracellular vesicles at single particle level. *Micro and Nano Systems Letters*, *10*, 14. https://doi.org/10.1186/s40486-022-00156-5

Lambert, T. J. (2019). FPbase: A community-editable fluorescent protein database. *Nature Methods*, *16*(4), 277–278. https://doi.org/10.1038/s41592-019-0352-8

Lambert, T. J. (2023). Using FPbase: The fluorescent protein database. In: Sharma, M. (eds) Fluorescent Proteins. *Methods in Molecular Biology*, *2564*, 1–45. https://doi.org/10.1007/978-1-0716-2667-2_1

Lee, K., Fraser, K., Ghaddar, B., Yang, K., Kim, E., Balaj, L., Chiocca, E. A., Breakefield, X. O., Lee, H., & Weissleder, R. (2018). Multiplexed profiling of single extracellular vesicles. *ACS Nano*, *12*(1), 494–503. https://doi.org/10.1021/acsnano.7b07060

Lennon, K. M., Wakefield, D. L., Maddox, A. L., Brehove, M. S., Willner, A. N., Garcia-Mansfield, K., Meechoovet, B., Reiman, R., Hutchins, E., Miller, M. M., Goel, A., Pirrotte, P., Van Keuren-Jensen, K., & Jovanovic-Talisman, T. (2019). Single molecule characterization of individual extracellular vesicles from pancreatic cancer. *Journal of Extracellular Vesicles*, *8*(1), 1685634. https://doi.org/10.1080/20013078.2019.1685634

Lozano-Andrés, E., Van Den Broeck, T., Wang, L., Mehrpouyan, M., Tian, Y., Yan, X., Arkesteijn, G. J. A., & Wauben, M. H. M (2024). Intrinsic variability of fluorescence calibrators impacts the assignment of MESF or ERF values to nanoparticles and extracellular vesicles by flow cytometry. *Nanomedicine: Nanotechnology, Biology, and Medicine*, *56*, 102720. https://doi.org/10.1016/j.nano.2023.102720

McNamara, R. P., Zhou, Y., Eason, A. B., Landis, J. T., Chambers, M. G., Willcox, S., Peterson, T. A., Schouest, B., Maness, N. J., MacLean, A. G., Costantini, L. M., Griffith, J. D., & Dittmer, D. P. (2022). Imaging of surface microdomains on individual extracellular vesicles in 3-D. *Journal of Extracellular Vesicles*, *11*(3), e12191. https://doi.org/10.1002/jev2.12191

Mladenović, D., Khamari, D., Kittel, Á., Koort, K., Buzás, E. I., & Zarovni, N. (2023). Acidification of blood plasma facilitates the separation and analysis of extracellular vesicles. *Journal of Thrombosis and Haemostasis*, *21*(4), 1032–1042. https://doi.org/10.1016/j.jtha.2023.01.007

Nieuwland, R., Enciso-Martinez, A., & Bracht, J. W. P. (2023). Clinical applications and challenges in the field of extracellular vesicles. *Medizinische Genetik*, *35*(4), 251–258. https://doi.org/10.1515/medgen-2023-2062

Nieuwland, R., & Siljander, P. R. (2024). A beginner's guide to study extracellular vesicles in human blood plasma and serum. *Journal of Extracellular Vesicles*, *13*(1), e12400. https://doi.org/10.1002/jev2.12400

Nolan, J. P., & Jones, J. C. (2017). Detection of platelet vesicles by flow cytometry. *Platelets*, *28*(3), 256–262. https://doi.org/10.1080/09537104.2017.1280602

Palviainen, M., Saraswat, M., Varga, Z., Kitka, D., Neuvonen, M., Puhka, M., Joenväärä, S., Renkonen, R., Nieuwland, R., Takatalo, M., & Siljander, P. R. M. (2020). Extracellular vesicles from human plasma and serum are carriers of extravesicular cargo—implications for biomarker discovery. *PLoS ONE*, *15*(8), e0236439. https://doi.org/10.1371/journal.pone.0236439

Saftics, A., Abuelreich, S., Romano, E., Ghaeli, I., Jiang, N., Spanos, M., Lennon, K. M., Singh, G., Das, S., Van Keuren-Jensen, K., & Jovanovic-Talisman, T. (2023). Single extracellular vesicle nanoscopy. *Journal of Extracellular Vesicles*, *12*(7), 12346. https://doi.org/10.1002/jev2.12346

Simonsen, J. B. (2017). What are we looking at? Extracellular vesicles, lipoproteins, or both? *Circulation Research*, *121*(8), 920–922. https://doi.org/10.1161/CIRCRESAHA.117.311767

Tian, Y., Gong, M., Hu, Y., Liu, H., Zhang, W., Zhang, M., Hu, X., Aubert, D., Zhu, S., Wu, L., & Yan, X. (2020). Quality and efficiency assessment of six extracellular vesicle isolation methods by nano-flow cytometry. *Journal of Extracellular Vesicles*, *9*(1), 1697028. https://doi.org/10.1080/20013078.2019.1697028

van der Pol, E., van Leeuwen, T. G., & Yan, X. (2021). Misinterpretation of solid sphere equivalent refractive index measurements and smallest detectable diameters of extracellular vesicles by flow cytometry. *Scientific Reports*, *11*(1), 24151. https://doi.org/10.1038/s41598-021-03015-2

van Niel, G., D'Angelo, G., & Raposo, G. (2018). Shedding light on the cell biology of extracellular vesicles. *Nature Reviews Molecular Cell Biology*, *19*(4), 213–228. https://doi.org/10.1038/nrm.2017.125

Varga, Z., Pol, E. v. d., Pálmai, M., Garcia-Diez, R., Gollwitzer, C., Krumrey, M., Fraikin, J.-L., Gasecka, A., Hajji, N., Leeuwen, T. G. v., & Nieuwland, R. (2018). Hollow organosilica beads as reference particles for optical detection of extracellular vesicles. *Journal of Thrombosis and Haemostasis*, *16*(8), 1646–1655. https://doi.org/10.1111/jth.14193

Vogel, R., Savage, J., Muzard, J., Della Camera, G., Vella, G., Law, A., Marchioni, M., Mehn, D., Geiss, O., Peacock, B., Aubert, D., Calzolai, L., Caputo, F., & Prina-Mello, A. (2021). Measuring particle concentration of multimodal synthetic reference materials and extracellular vesicles with orthogonal techniques: Who is up to the challenge? *Journal of Extracellular Vesicles*, *10*(3), e12052. https://doi.org/10.1002/jev2.12052

Weiss, R., Mostageer, M., Eichhorn, T., Huber, S., Egger, D., Spittler, A., Tripisciano, C., Kasper, C., & Weber, V. (2024). The fluorochrome-to-protein ratio is crucial for the flow cytometric detection of tissue factor on extracellular vesicles. *Scientific Reports*, *14*(1), 6419. https://doi.org/10.1038/s41598-024-56841-5

Welsh, J. A., Arkesteijn, G. J. A., Bremer, M., Cimorelli, M., Dignat-George, F., Giebel, B., Görgens, A., Hendrix, A., Kuiper, M., Lacroix, R., Lannigan, J., van Leeuwen, T. G., Lozano-Andrés, E., Rao, S., Robert, S., de Rond, L., Tang, V. A., Tertel, T., Yan, X., … van der Pol, E. (2023). A compendium of single extracellular vesicle flow cytometry. *Journal of Extracellular Vesicles*, *12*(2), e12299. https://doi.org/10.1002/jev2.12299

Welsh, J. A., Goberdhan, D. C. I., O'Driscoll, L., Buzas, E. I., Blenkiron, C., Bussolati, B., Cai, H., Di Vizio, D., Driedonks, T. A. P., Erdbrügger, U., Falcon-Perez, J. M., Fu, Q., Hill, A. F., Lenassi, M., Lim, S. K., Mahoney, M. G., Mohanty, S., Möller, A., Nieuwland, R., … Witwer, K. W. (2024). Minimal information for studies of extracellular vesicles (MISEV2023): From basic to advanced approaches. *Journal of Extracellular Vesicles*, *13*(2), e12404. https://doi.org/10.1002/jev2.12404

Welsh, J. A., Jones, J. C., & Tang, V. A. (2020). Fluorescence and light scatter calibration allow comparisons of small particle data in standard units across different flow cytometry platforms and detector settings. *Cytometry Part A: The Journal of the International Society for Analytical Cytology*, *97*(6), 592–601. https://doi.org/10.1002/cyto.a.24029

Welsh, J. A., Van Der Pol, E., Arkesteijn, G. J. A., Bremer, M., Brisson, A., Coumans, F., Dignat-George, F., Duggan, E., Ghiran, I., Giebel, B., Görgens, A., Hendrix, A., Lacroix, R., Lannigan, J., Libregts, S. F. W. M., Lozano-Andrés, E., Morales-Kastresana, A., Robert, S., De Rond, L., … Jones, J. C. (2020). MIFlowCyt-EV: A framework for standardized reporting of extracellular vesicle flow cytometry experiments. *Journal of Extracellular Vesicles*, *9*(1), 1713526. https://doi.org/10.1080/20013078.2020.1713526

Zhu, J., Wu, F., Li, C., Mao, J., Wang, Y., Zhou, X., Xie, H., & Wen, C. (2023). Application of single extracellular vesicle analysis techniques. *International Journal of Nanomedicine*, *18*, 5365–5376. https://doi.org/10.2147/IJN.S421342

SUPPORTING INFORMATION

Additional supporting information can be found online in the Supporting Information section at the end of this article.

How to cite this article: Mladenović, D., Brealey, J., Peacock, B., Koort, K., & Zarovni, N. (2025). Quantitative fluorescent nanoparticle tracking analysis and nano-flow cytometry enable advanced characterization of single extracellular vesicles. *Journal of Extracellular Biology*, *4*, e70031. https://doi.org/10.1002/jex2.70031